A Medical Imaging Demonstrator of Computed Tomography and Bone Mineral Densitometry

Thomas Claesson

Stockholm 2001

Royal Institute of Technology
Department of Physics

Master of Science Thesis

Department of Physics
Royal Institute of Technology
Stockholm, Sweden

Claesson, Thomas: A Medical Imaging Demonstrator of Computed Tomography and Bone Mineral Densitometry.

TRITA 9119
ISSN 0280-316X

© Thomas Claesson, July 2001

Printed by: Universitetsservice US AB, Stockholm 2001

Abstract

A demonstrator of two different medical imaging techniques employed in clinical practise has been designed and built for educational purposes. The set-up demonstrates Computed Tomography and Bone Mineral Density measurement using the Dual Photon Absorption method. The system is based on a solid state CdZnTe detector and a standard PC. The mechanics of the system is controlled and data is acquired by programs written in LabView. Computed Tomography images are reconstructed using MATLAB programs.

Contents

Chapter 1 **Introduction** 5
- **1.1 Motivation** 5
- **1.2 Bone Mineral Density measurement** 5
- **1.3 Computed Tomography** 6

Chapter 2 **Interaction of gamma radiation with matter** 9
- **2.1 Different types of interaction** 9
  - *2.1.1 Photoelectric effect* 9
  - *2.1.2 Compton scattering* 10
- **2.2 Absorption of low energy gamma radiation in matter** 11

Chapter 3 **Computed Tomography** 13
- **3.1 Background and motivation** 13

3.2 The principles of Computed Tomography 14
3.3 Mathematics of image reconstruction 16
3.3.1 Definition of geometry 16
3.3.2 Image reconstruction methods 18
3.4 Implementation 18

Chapter 4 **Bone Mineral Density measurement** **21**
4.1 Background and motivation 21
4.2 Principles of Bone Mineral Density measurement 21
4.2.1 Dual photon absorptiometry 22

Chapter 5 **The X-ray detector** **25**
5.1 Background 25
5.1.1 Semiconductor detectors in general 25
5.2 Quantifying detector performance 26
5.3 The CdZnTe semiconductor detector 26
5.4 Defects and trapping 28

Chapter 6 **The ^{241}Am gamma ray source** **31**
6.1 Decay and spectrum 31
6.2 Activity and shielding 33

Chapter 7 **Description of the set-up** **35**
7.1 Moving parts 35
7.2 Electrical stepper motors 37
7.3 Stepper motor control boards 37
7.4 Nuclear electronics modules 37
7.5 Data acquisition procedure 39
7.6 PC software 40

Chapter 8 **Results** **41**
8.1 Counting statistics 41
8.2 CT images 42
8.2.1 Spatial resolution 42
8.2.2 Energy selection and contrast level 43
8.2.3 Distortions of the reconstructed image 45
8.2.4 Acquisition time 46
8.3 Bone Mineral Density profiles 47

References **51**

Chapter 1

Introduction

1.1 Motivation

The Nuclear Physics group of the Physics Department at the Royal Institute of Technology is responsible for an undergraduate course in medical imaging. In this course techniques based on ionising radiation as well as other phenomena are treated, for instance conventional radiology with X-rays, X-ray Computed Tomography (CT), Magnetic Resonance Imaging (MRI), Nuclear medicine using Gamma camera and Positron Emission Tomography (PET). The students make visits to hospital clinics where they can see how these instruments are used in clinical practice. However, when you see for instance a Computer Tomograph in such a situation it looks very much like any other advanced imaging equipment and it is difficult to get an understanding of how it really works.

To achieve a better understanding the students do lab exercises where they get hands-on-experience of detectors and the signals and spectra that they produce. To illustrate more complex applications two other experimental set-ups have previously been developed – a digital Multi Wire Proportional Chamber X-ray imaging system and a Time Of Flight PET-camera. The TOF-PET set-up was developed in another diploma work project. This demonstrator of X-ray Computed Tomography and Bone Mineral Density measurement will complement the other lab exercises as an educational tool. The purpose is hence not to achieve high capacity in terms of good spatial resolution and short acquisition times, but to be instructive and transparent. The students can during the whole process of data acquisition see where X-ray source and the detector are in relation to the examined object as well as how each new data is registered in real time. The physical process that explains these two techniques is absorption of low energy gamma radiation in matter.

1.2 Bone Mineral Density measurement

Among the population of elderly women a common disease is Osteoporosis. This disease means that there is a decrease in the total amount of skeletal bone, which leads to a increasing risk of fractures [1]. Besides the pain and suffering of the individual this leads to high economical costs for the society since a large number fractures are caused by this disease. Therefor a diagnostic method able of telling whether a patient is suffering from osteoporosis or not is very important. Such a method makes it possible to start a treatment that can increase the bone mineral density to a level where the risk of fractures is reduced. Several such methods exist, some of them being based on of absorption of X-rays.

In this set-up a demonstration of the Dual Photon Absorption (DPA) method is implemented. This method is based on the fact that absorption of X-rays in any material, for instance bone mineral and soft tissue like fat and muscle, is a function of the X-ray energy as well as the material itself. Using this fact it is possible to separate the contribution to the X-ray absorption due to bone from that due to soft tissue if the transmitted X-ray intensity is measured at two different discrete energies.

1.3 Computed Tomography

In 1895 the German physicist Wilhelm Röntgen made the truly revolutionary discovery of X-rays and how they could be used for imaging. Immediately scientists all over the world realised the enormous potential of this new technique and six years later Röntgen was awarded the very first Nobel prize in physics for this discovery. This was the first technique for imaging the inside of the body and has since then been an invaluable diagnostic tool at hospital clinics all over the world.

The methods and the equipment for conventional medical imaging with X-rays used today, more than one hundred years later, are actually more or less the same. Of course there has been technical progress, for instance X-rays tubes and image receptors have become more efficient resulting in reduction of the dose necessary to give to the patient. However, the image quality in terms of spatial resolution and level of contrast is roughly the same as it was in the early days of the 20:th century. The next revolutionary discovery in the field of medical imaging with X-rays arrived in the beginning of the 1970:s when the first equipment for Computed Tomography (CT) was developed. This method of imaging avoids several important limitations that conventional X-ray radiology suffers from. It produces images depicting the body in a completely new way with a contrast discrimination up to one thousand times better than that of a conventional radiograph. In just a few years CT was established as a clinically applied imaging technique all over the world, its importance being confirmed by the 1979 Nobel prize in Medicine or Physiology awarded to the two most important inventors, Allan M Cormack and Godfrey N Hounsfield [2].

The differences between CT imaging and conventional radiography are several and important. The most important aspect is that CT improves image quality in a number of ways, these issues will be discussed in more detail in chapter 3, Computed Tomography. There is also a number of differences of technical and practical nature.

In a CT machine the X-ray intensity is registered by an array of detectors for gamma radiation, while the image receptor in conventional radiography is a photographic film with layers of fluorescent material sensitive to X-rays. When the radiographic film has been developed it is also used as storage media. After CT data acquisition the image is not available immediately but must be calculated, reconstructed, by a computer with the help of a complex algorithm. A CT system has the advantage that the image is digitised from the beginning and hence is available for digital storage or image processing on a computer. From a set of different CT slices it is even possible to generate a three-dimensional computer reconstruction of a part of the body.

Chapter 2

Interaction of gamma radiation with matter

2.1 Different types of interaction

Gamma radiation encountering matter experiences mainly three different types of basic interactions, namely photoelectric effect, Compton scattering and pair production. Depending on the energy of the radiation different processes will dominate. At low energies the photoelectric effect dominates while at intermediate energies the Compton scattering is the most important and finally at high energies the pair productions mechanism will dominate. In the energy range considered here, i.e. relatively low energies between 10 and 60 keV, clearly the photoelectric effect is the dominating process [3,4].

2.1.1 Photoelectric effect

The photoelectric effect is the complete absorption of an incoming photon upon interaction with an atomic electron. All the energy of the photon is transferred to the electron, which is emitted from the atom with an energy Te given by

$$T_e = E_\gamma - E_b \tag{2.1}$$

, where E_γ is the energy of the photon and E_b is the atomic binding energy of the electron. From this relation it is obvious that a requirement for photoelectric effect to be possible is that the photon energy exceeds the atomic binding energy of the electron. This requirement is clearly visible in a plot of the photoelectric crossection, σ, as a function of photon energy, see figure 2.1 below.

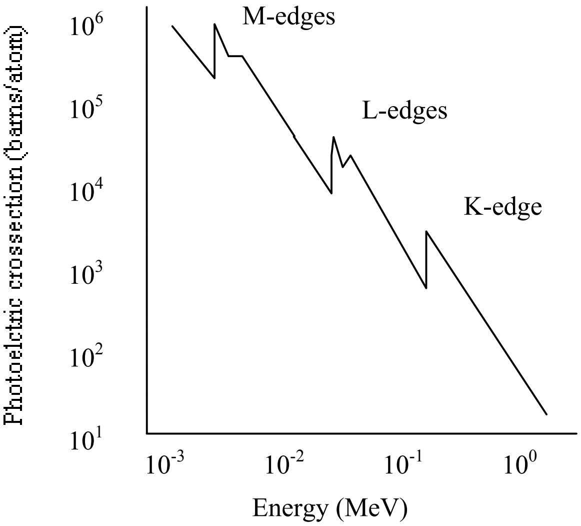

Figure 2.1. Schematic plot of the photoelectric crossection in lead as a function of photon energy.

The points where the crossection increases dramatically, the so-called edges, correspond to the atomic binding energies of the different electronic shells (K-shell, L-shell and so on). When the photon energy is high enough to ionise electrons in a shell where they are more tightly bound, there is a discontinuous increase of the crossection. These edges are called the L-absorption edges, M-absorption edges and so on.

Treating the photoelectric effect theoretically is quite a difficult task, however the following relation for the photoelectric cross section σ_e is approximately true

$$\sigma_e \propto E_\gamma^{-a} Z^b \qquad (2.2)$$

, where E_γ is the energy of the photon and Z is the atomic number of the absorbing material. The exponents a and b vary with energy and atomic number but can be approximated to $a \approx 3$ and $b \approx 4.5$ [3,4].

2.1.2 Compton scattering

The Compton scattering process is the scattering of photons on initially free electrons. There are of course no free electrons in matter, but if the photon energy is large compared to the binding energy of the electron, then the electron can be considered as free [3,4]. The photon is not absorbed, it just loses some energy and continues after a change of direction. The kinematics of the interaction is illustrated in figure 2.2 below.

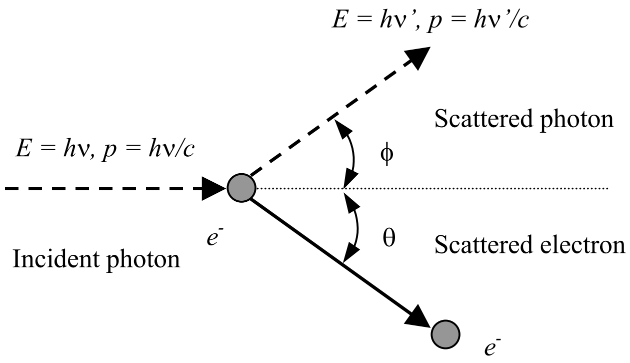

Figure 2.2. The kinematics of the Compton effect.

Applying the conditions of conservation of energy and momentum it is possible to show that the energy of the scattered photon will be

$$h\nu' = \frac{h\nu}{1 + \frac{h\nu}{m_e c^2}(1 - \cos\phi)} \tag{2.3}$$

2.2 Absorption of low energy gamma radiation in matter

As a result of the interactions described above the photons are either Compton scattered with some loss of energy or completely absorbed in a photoelectric interaction. This means that if a well collimated beam of photons is considered, photons will disappear from the beam as a result of interactions. Only those photons that have not undergone any interactions at all remain in the beam, which means that a beam of photons is not degraded in energy as a result of passing through matter, just attenuated in intensity (number of photons per unit time and unit area). Considering a slab of matter of thickness dx and atomic density n_a ($n_a = N_A\rho/A$, where N_A is Avogadro's number, ρ is the mass density A and is the atomic weight) the areal density of atoms is $n_a dx$. If the total interaction crossection per atom is σ, then the interaction probability for each photon incident on the slab will be na σdx. For a beam of intensity I the total attenuation is

$$-dI = I\, n_a\, \sigma\, dx \tag{2.4}$$

, which after integration gives

$$I(x) = I(0)*exp(-n_a\sigma x) = I(0)*exp(-\mu x) \tag{2.5}$$

, where the linear attenuation coefficient μ has been defined according to $\mu = n_a\, \sigma$ and has units of 1/length, for instance cm^{-1}. In other words equation (2.4) above says that the linear attenuation coefficient μ is the fractional change in intensity of the incident beam per unit thickness of the attenuating material [3,4]. Since the linear attenuation coefficient is proportional to the crossection per atom, σ, it is a function of both the energy of the photons and the elemental composition of the attenuating material. This is a fact that medical imaging with photons relies on.

Chapter 3

Computed Tomography

3.1 Background and motivation

As mentioned in section 1.3, X-rays have been used for imaging the human body all since their discovery more than one hundred years ago. The basic physical principle behind X-ray imaging is the interaction of X-ray photons with matter, as previously described in chapter 2. The image receptor in conventional radiography is a special type of film emulsion mounted inside a cassette together with a layer of fluorescent material sensitive to X-rays. The film is exposed, blackened, by the light created when radiation hits the fluorescent material but remains transparent if little or no radiation is transmitted through the patient. The absorption of X-rays in the body as well as in the fluorescent material of the film cassette is governed by the expression given in equation (2.5). Since the linear attenuation coefficient μ is a function of the material density and the atomic number Z, it is different for different types of matter found in various parts of the body, see table 3.1 below [5].

Air	Bone	Muscle	Blood
0	0.48	0.18	0.178

Table 3.1. Linear attenuation coefficients in cm^{-1} of compounds of the human body for the energy spectrum of a typical X-ray beam used in medical imaging.

This is what gives the contrast in a radiograph; one cm of bone will attenuate the beam much more than an equal amount of muscle and therefor the bone structure will have a brighter contrast than muscle in the radiograph. However the difference in contrast visible on an ordinary radiographic film is limited, in principle the radiologist essentially discriminates between a small number of compounds like air, bone, soft tissue (fat and muscle) and water. This is one of the fundamental limitations of conventional radiography, it is impossible to see details like the blood in the blood vessels or the structure of the heart anatomy.

Conventional radiographs are projections where the depth dimension is lost, organs lying behind each other cannot be separated. In other words, a conventional radiograph is a two-dimensional representation of a part of the three-dimensional human anatomy. Exact localisation of features in the image requires taking two pictures perpendicular to each other. A CT image on the other hand is a crossectional image showing a slice of the body just a few millimetres thick. The two-dimensional CT image depicts an equally two-dimensional section of the body and no spatial dimension is lost [5,6,7,8,9].

Because the X-ray beam in conventional radiography is divergent, geometrical distortions are introduced in the image, organs lying on different depth inside the body are magnified differently. No such distortions are present in a CT image.

All these basic problems of X-ray imaging were at once solved with the invention of Computed Tomography about 30 years ago.

3.2 The principles of Computed Tomography

The word tomography comes from the two Greek words *tomos* (cut) and *graph* (written) and means sectional imaging, a crossectional slice of the body is defined and depicted. Over the years several techniques have been developed for tomography with ordinary X-ray film, but none of them has shown satisfying results. However, using a modern Computed Tomography (CT) scanner a tomogram showing the human anatomy with a position resolution of about 1 mm and a contrast discrimination several orders of magnitude better than that of conventional radiography is easily achieved [5].

Conventional X-ray imaging makes use of a single wide beam emerging from the focal spot inside the X-ray tube. The beam diverges so that it covers the entire object to be imaged and hence the entire film. In Computed Tomography the film emulsion is replaced by one or several X-ray detector(s) whose output signals are fed into a data acquisition system and stored in the memory of a computer. Radiation is only transmitted through the body in the plane of the slice being imaged. Instead of using a single wide beam a number of narrow so-called pencil beams are swept in many different directions over the imaged plane. The data set acquired consists of the measured values of the X-ray intensity transmitted through the patient for various positions and directions of the source-detector configuration. The image is finally reconstructed, that is calculated, by the computer applying a mathematical transformation to the data set and the result is displayed on a computer screen [7,8,9].

The first type of CT scanners, also referred to as the first generation, that were constructed in the beginning of the 1970:s perform data acquisition using a single detector and a source of pencil beam X-rays, that are scanned sideways across the image plane, see figure 3.1 below.

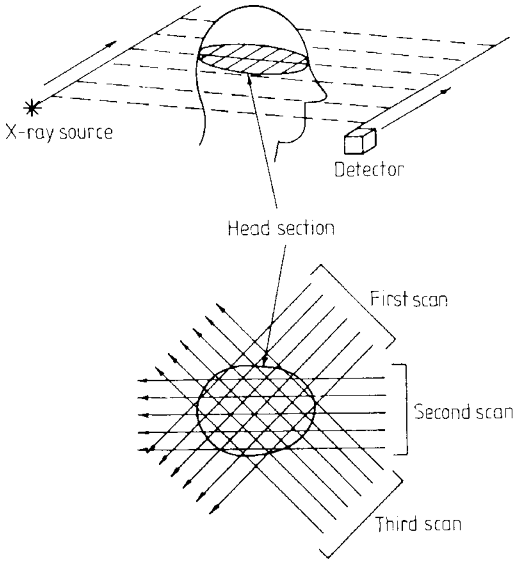

Figure 3.1. Schematic illustration to the source-detector configuration used in the first generation of CT scanners.

When the entire image plane has been scanned the source and detector are rotated a small angle and the procedure of scanning sideways is repeated again. This is the so-called parallel beam geometry. The set of attenuation data for a certain angle is called a parallel projection. When parallel projections for a complete half revolution are acquired there is enough data to reconstruct the image.

To speed up data acquisition, more efficient types of CT scanners have been developed over the years. These developments in detector geometry are shown from the first through the fourth generation of scanners in figure 3.2 below

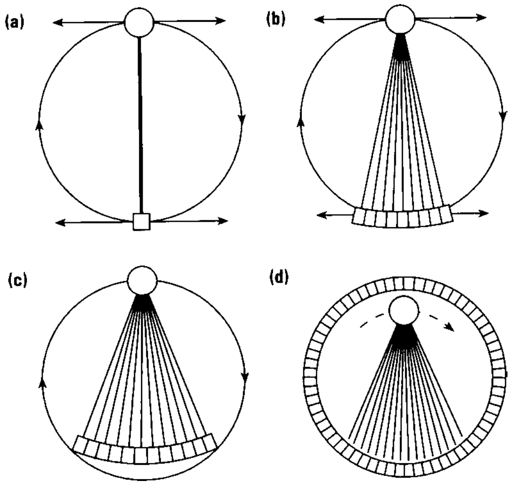

Figure 3.2. Schematic representation of the source-detector configuration of all the four different generations of CT scanners. (a) First generation, (b) second generation, (c) third generation, (d) fourth generation.

From the second generation and further on the single detector is replaced by a detector array and the parallel beam geometry is turned into a divergent fan beam geometry. Going from the first generation to the second the source-detector configuration still needs to be both rotated and translated, but fewer angular steps are needed to acquire the complete data set. In the third generation the detector array has several hundred detector elements and rotates continuously around the patient without translation. In the fourth generation the detector array covers the hole circle around the patient and the X-ray tube alone rotates [6].

A very crucial step in Computed Tomography is the calculation of the image from the acquired data set of projections. Hounsfield and Cormack were actually not the first to think of this problem, already in 1917 the Austrian mathematician Johann Radon showed that it is possible to reconstruct a crossectional image of an unknown object using an infinite number of projections through the object. In honour of Radon the projection of a two-dimensional object in a certain direction is called the Radon transform of the object. In computed tomography the goal is to do the inverted process, that is going from a set of projection data back to the original object, which hence is called the inverse Radon transform.

3.3 Mathematics of image reconstruction

As mentioned above the resulting CT image needs to be reconstructed from the acquired data set by calculations performed by a computer. In this section the mathematics of image reconstruction in Computed Tomography will be described. The derivation of course depends on the geometry considered, the simplest case being the parallel beam geometry of the first generation of CT scanners. Since the additional complexity of fan beam geometry adds nothing essential to the basic understanding of the principles, only parallel beam geometry will be considered here.

3.3.1 Definition of geometry

What is the mathematical description of the parallel projections described in section 3.1? First of all two different coordinate systems have to be defined, one that is fixed in the object being X-rayed (x,y) and another that rotates with the source and detector (x',y'), see figure 3.3 below describing a general two-dimensional distribution $f(x,y)$.

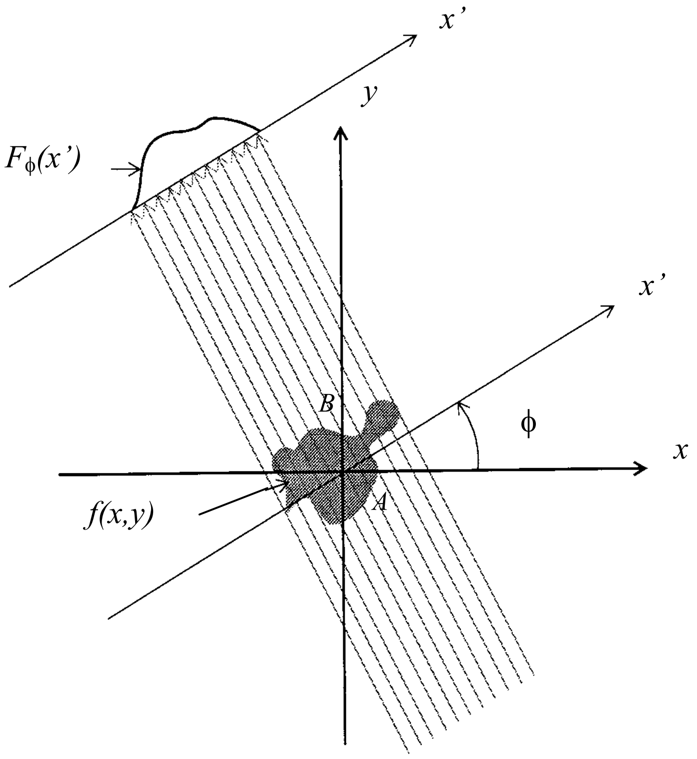

Figure 3.3. The geometry and coordinate systems that define parallel projections for a general two-dimensional distribution f(x,y).

Going from the general case to the situation in CT imaging, the two-dimensional distribution to be measured is that of the linear attenuation coefficient $\mu(x,y)$. For a certain angle, ϕ, the source of X-rays and the detector are translated along the x' axis and the parallel projection $F_\phi(x')$ is built up point by point.

Each data point in a parallel projection is a measure of the attenuation of X-ray beams of a specific energy along a straight line *AB*. The linear absorption coefficient, μ, is a function of the y' coordinate along *AB* and each infinitesimal element dy' gives a contribution to the total attenuation of the X-ray beam. The transmitted intensity measured is the sum of all those infinitesimal contributions and hence a line integral along *AB*.

If the following assumptions are made:
(i) the X-ray beam is a narrow pencil beam
(ii) the radiation is monoenergetic
(iii) none of the scattered radiation hits the detector
then the transmitted X-ray intensity along a specific line *AB* is given by the expression

$$I_\phi(x') = I_\phi^0(x')e^{-\int_{AB}\mu(x,y)dy'} \tag{3.1}$$

, where *AB* is a straight line parallel to the *y'* axis located at the distance *x'* from the origin and ϕ is the angle between the *(x,y)* and *(x',y')* frames. From this expression the projection of the object measured at an angle ϕ and distance *x'* is defined as

$$F_\phi(x') = -\ln(I_\phi(x')/I_\phi^0(x')) = \int_{-\infty}^{\infty}\int_{-\infty}^{\infty}\mu(x,y)\delta(x\cos\phi + y\sin\phi - x')dxdy \tag{3.2}$$

These are the line integrals that make up the projection sets. Since the equation of the straight line *AB* is $x' = x\cos\phi + y\sin\phi$, the Dirac delta function indicates that the integration is carried out only along the line *AB*. To calculate the image this relation must be inverted so that $\mu(x,y)$ is recovered from the projection set $F_\phi(x')$. This operation is called image reconstruction and from equation (3.2) it is obvious that this is not a trivial task with a general solution [5].

3.3.2 Image reconstruction methods

A number of different methods for image reconstruction exist, each with its benefits and drawbacks. The major difference is between the convolution and backprojection methods on one side and the iterative methods on the other hand.

The iterative methods involve solving a large number (typically 10^5) of equations simultaneously. The solution is accepted if a certain criteria is fulfilled. If that is not the case the values are changed according to some algorithm and by iteration a new solution is found and tested. These methods are quite computer intensive and therefor not used in commercial systems.

A commonly applied method in the convolution and backprojection category is the so-called 'filtered backprojection' algorithm. It relies on the Fourier slice theorem, which in effect states that it is possible to reconstruct an object from a set of projections provided that projection data set contains enough information. By enough information is meant that the projections must be taken for a large number of angles over a complete half revolution (180°). This method involves Fourier transformation of the data set with respect to spatial coordinates (*x'* and ϕ). Statistical fluctuations are of course more or less always present in any data set. After Fourier transformation of a data set these fluctuations will appear as high-frequency noise in the spatial frequency domain. One drawback of this method is that such high-frequency components are amplified unproportionally. To reduce the effect of this amplification different filters are applied. Such a filter is a mathematical function that the data is multiplied by in the process of transformation. Commonly used filters are for instance Ramachandran-Lakshminarayanan, Shepp-Logan, Hamming, Hann and Butterworth [5,6,7,8,9].

3.4 Implementation

This demonstrator has adopted the principles of the first generation of CT scanners, a parallel beam geometry and a rotate-translate pattern of movements. To further simplify the construction it is the object to be imaged, the ”patient”, that is rotated – not the detector and X-ray beam source. The following two figures schematically illustrate an actual case of CT data acquisition with this demonstrator using an object consisting of three different cylindrical solid rods. The thinnest rod is made of steel, which due to its high linear attenuation coefficient absorbs the low energy photons almost completely.

The two thicker rods are made of a transparent plastic material, which has a much lower linear attenuation coefficient and consequently absorbs less.

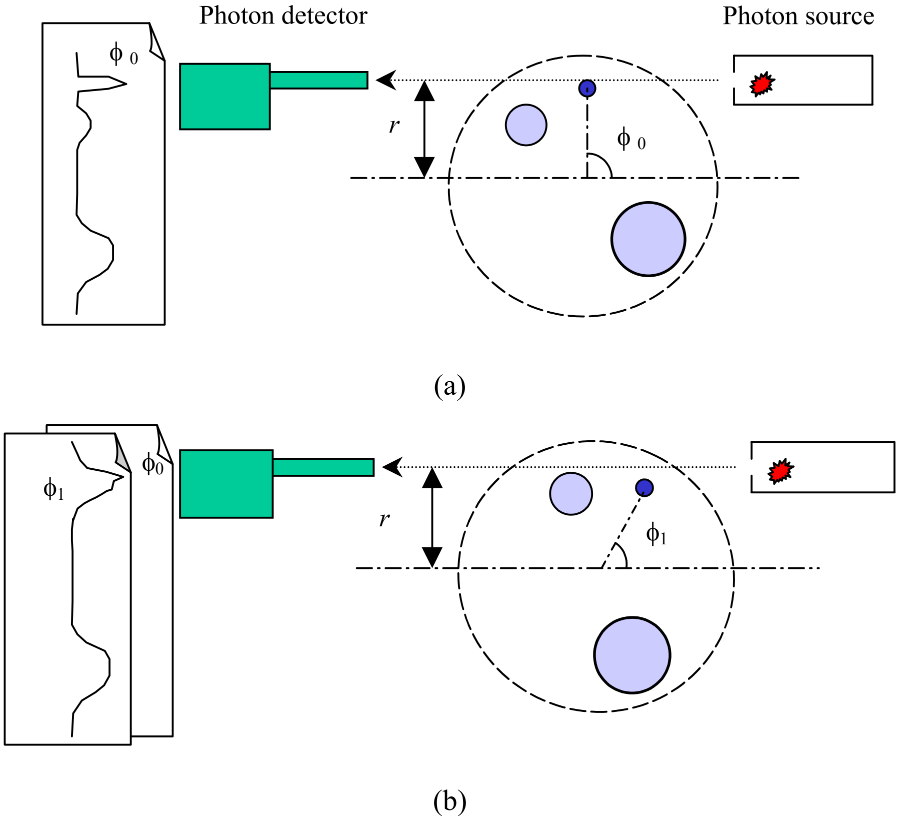

Figure 3.4a & b. Schematic illustration to CT data acquisition as it is implemented in this demonstrator. The object is a phantom, i.e. a reference object, consisting of three solid cylindrical rods of different sizes and materials.

Figure 3.4a shows the situation for a certain angle, ϕ_0, while figure 3.4b shows what has happened after rotation through an angle $\Delta\phi$. To the left the graph of the transmitted photon intensity as a function of the vertical distance, *r*, is shown. The two broad peaks in the graph of figure 3.4a are caused by the plastic rods, while the sharp peak indicating strong absorption is caused by the narrow steel rod. In figure 3.4b, when the object has rotated to the next angle, ϕ_1, two of the rods are in front of each other. In the transmission graph this results in merged peaks.

Denoting the number of distinct vertical positions by *m* and the number of angles, covering half a revolution (180°), by *n*, the total data set is a two-dimensional *m* x *n* matrix. This matrix is commonly displayed as a two-dimensional pseudo colour plot, which is called the sinogram. The vertical and horizontal axis of the sinogram indicate the vertical position, *r*, and the angle ϕ, respectively. The sinogram is shown in figure 3.5 below for the three rod phantom illustrated above. The three different rods are easily identified by their different sizes. From the grey level of the lines it is also seen that the absorption in the thick plastic rod is greater than in the thin one despite that they are of the same material, as it should be.

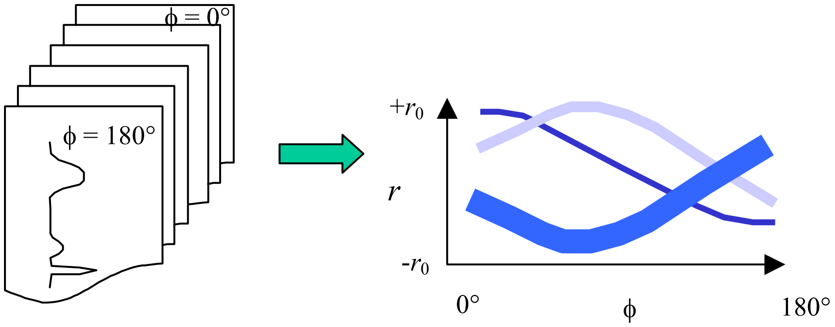

Figure 3.5. Illustration to how the different parallel projections for all angles between 0° and 180° together form the sinogram.

Chapter 4

Bone Mineral Density measurement

4.1 Background and motivation

Osteoporosis is a disease where the absolute amount of skeletal bone decreases dramatically. This results in an increased risk of fractures as a consequence of minimal traumas and normal stress. The actual size, and hence the volume, of the bone remains unchanged, but the cortical regions get thinner and the bone shows porosis. There is less specific bone tissue in relation to bone marrow and the additional space created is filled with fat. As far as the chemical composition is concerned osteoporotic bone is not distinguishable from normal and the relationship between organic matter and mineral is unchanged. These characteristics of the disease make diagnostics with X-rays an ideal tool for quantifying the amount of bone mineral in a certain part of the body, for instance the forearm [1].

4.2 Principles of Bone Mineral Density measurement

To make a quantitative measurement of the bone mineral density of for instance the forearm it is not sufficient to just let a monoenergetic X-ray beam penetrate the arm and measure the transmitted intensity. The reason for this is that the X-rays will of course be attenuated by both bone and soft tissue (muscle and fat) and hence it is impossible to separate the attenuation due to bone from that due to soft tissue.

One approach to this problem is to embed the examined body part in some material that resembles muscle and other types of soft tissue in terms of X-ray attenuation, for instance water. In this way the thickness of soft tissue and soft tissue equivalent material surrounding the bone is constant. The absorption profile will then show a fixed base line due only to absorption in soft tissue and the surrounding material (water). Absorption due to bone will show up above this base line [1].

However there are of course some parts of the body that cannot easily be surrounded by a constant thickness of soft tissue equivalent material, which for instance is the case when the bone mineral density of the lumbar spine or femur is to be measured. A method that doesn't require extra material surrounding the body part is the so-called Dual Photon Absorptiometry (DPA). The principle of DPA is to use two different discrete X-ray energies and measure the transmitted intensity of both. What makes it possible to separate the attenuation due to soft tissue from that due to bone is the dependence of the linear attenuation coefficient on energy and material, see chapter 2 and figure 4.1 below.

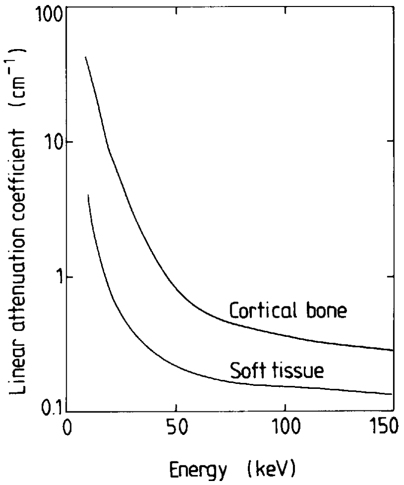

Figure 4.1. Linear attenuation coefficients in cm^{-1} of soft tissue and cortical bone as a function of energy.

4.2.1 Dual photon absorptiometry

As described in chapter 2 the linear attenuation coefficient is proportional to the density of the material. As an illustration to this, consider that

$$\mu_{water} > \mu_{ice} > \mu_{water\ vapour} \tag{4.1}$$

Sometimes it is useful to eliminate the dependence of density from the linear attenuation coefficient and for that purpose the so-called mass attenuation coefficient μ_m is defined as

$$\mu_m = \mu / \rho \tag{4.2}$$

where μ is the linear attenuation coefficient and ρ is the mass density. If ρ is expressed in units of g/cm^3 and μ in cm^{-1}, then μ_m will have units of cm^2/g. Since the dependence of physical density is removed from μ_m it only depends on the energy of the photons and the elemental composition of the attenuating material. Using the mass attenuation coefficient the expression for attenuation of X-rays is

$$I(x) = I(0)*exp(-\mu_m \rho x) \tag{4.3}$$

where the quantity ρx is the areal density in units of g/cm^2. A physical interpretation of the areal density is the total mass of a column of unit cross-sectional area being penetrated by the X-rays. This figure is what is routinely being measured at a clinical Bone Mineral Density (BMD) scan.

When an X-ray beam penetrates for instance the forearm it is attenuated by soft tissue with linear attenuation coefficient μ_s and areal density $\rho_s x_s$ as well as by bone mineral with linear attenuation coefficient μ_b and areal density $\rho_b x_b$. Dual photon absorptiometry

(DPA) relies on the use of two different X-ray energies. Letting primed (’) variables denote the low energy radiation and unprimed denote the high energy, these equations describe the absorption:

$$I' = I_0'*exp-(\mu_s'\rho_s x_s+\mu_b'\rho_b x_b) \qquad (4.4a)$$

$$I = I_0*exp-(\mu_s\rho_s x_s+\mu_b\rho_b x_b) \qquad (4.4b)$$

With the definition $J = -ln(I/I_0)$ it is possible to write these expressions as a linear system of equations:

$$J' = \mu_s'\rho_s x_s+\mu_b'\rho_b x_b \qquad (4.5a)$$

$$J = \mu_s\rho_s x_s+\mu_b\rho_b x_b \qquad (4.5b)$$

Solving these two equations simultaneously for the areal densities of bone and soft tissue respectively yields [1]

$$\rho_b x_b = \frac{J'-(\mu_s/\mu_s)J}{\mu_b' - (\mu_s'/\mu_s)\mu_b} \qquad (4.6a)$$

$$\rho_s x_s = \frac{(\mu_b'/\mu_b)J - J'}{(\mu_b'/\mu_b)\mu_s - \mu_s'} \qquad (4.6b)$$

Certain requirements must be fulfilled for this method to be applicable. For instance the values of the four attenuation coefficients (bone and soft tissue for low and high energy) must be known. This presents a problem since the composition of soft tissue varies between different individuals. Another requirement lies in the choice of energies. To obtain a measurable difference in attenuation there must be a minimum difference between the two energies used.

Chapter 5

The X-ray detector

5.1 Background

As gamma and X-ray radiation penetrates matter it interacts according to the processes described in chapter 2. The result of for instance Compton scattering and photoelectric effect is free electrons leaving the interaction point with some energy and atoms left behind that lack one or more electrons, i.e. the radiation is ionising. In many types of detectors for ionising radiation the basic principle of operation is to detect the free charge created in this process. There exists a wide variety of different detectors for different types of radiation and energy ranges based on different principles. Since this set-up relies on a semiconductor detector, only these detectors will be discussed.

5.1.1 Semiconductor detectors in general

The sensitive volume of a semiconductor detector is a solid block of some semiconductor material. Like in an ordinary *pn*-junction a *p*-type region is brought in contact with an *n*-type region forming a diode with an electric field and a depleted region between the *n* and *p*-type regions. When the detector is in operation a reverse bias is applied across the diode, increasing the dimensions of the depleted region and the magnitude of the electric field [3,4,10].

When ionising radiation enters the depleted region, free charge carriers, electrons and holes, are created as the radiation interacts with the semiconductor atoms. Under the influence of the electric field electrons and holes will drift towards the oppositely charged electrodes, the electrons towards the anode and the holes towards the cathode. The number of electron-hole-pairs created in an ionising event is simply equal to the energy deposited in the material divided by the energy required to create a single electron-hole-pair. The movement of charge carriers towards the electrodes gives rise to a transient current. This current has one contribution from the electrons and another from the holes and since the mobility of electrons in general is different from that of the holes, these two contributions will also be different.

In many applications it is not enough just to know that an interaction has occurred, it is also of interest to know the energy of the radiation. Since it is the total charge created in the depleted region that gives the deposited energy, the transient current needs to be integrated. That integration is made by a so-called charge sensitive preamplifier, which on its output gives a voltage pulse with an amplitude proportional to the time integral of the transient current [10].

Semiconductor materials commonly used in nuclear physics applications are germanium (Ge) and silicon (Si). Ge has to be cooled down to liquid nitrogen temperature (77K) for best operating performance, while only some Si detectors must be cooled during operation.

5.2 Quantifying detector performance

Two important measures of detector performance are the energy resolution and the intrinsic detection efficiency.

The energy resolution of a detector is a measure of its ability to separate two close lying energies from each other. In an ideal case monoenergetic radiation penetrating a detector would result in a very narrow delta-peak in the output spectrum. However, in a real case this is not true because of several reasons. Features like statistical fluctuations in the generation and collection of charge as well as electronic noise influence the signal. The result is instead a peak of Gaussian shape having a certain non-zero width. Energy resolution is usually given in terms of full width at half maximum (FWHM). Two peaks of equal intensity lying closer than the FWHM are not considered resolvable, they will just look like a single peak in the output spectrum [4].

The intrinsic efficiency is simply the fraction of events hitting the detector that are registered and produce a measurable output signal. It depends not only on the detector material, but also on the type of radiation and its energy. For gamma/X-ray detectors the dimensions of the sensitive volume are important since the interactions are quite rare and a large volumes increases the probability of interaction [4].

5.3 The CdZnTe semiconductor detector

A detector used in this experimental set-up needs to fulfil some basic requirements. Since photons in the region 10 – 60 keV are used, the detector must have a high intrinsic efficiency and an acceptable energy resolution in that energy range. Since the detector must be mounted on a moveable arm it cannot be too big and heavy so liquid nitrogen cooling is therefor excluded. All these requirements are met by a relatively recently commercially available detector, a CdZnTe compound semiconductor detector.

This detector, sometimes referred to as just CZT, has a high intrinsic efficiency in the energy range 5 – 75 keV, see figure 5.1 below where the interaction probability is plotted as a function of photon energy. In general the intrinsic efficiency is a function of the interaction probability and the geometry of the detector. The interaction probability is hence not the same thing as the intrinsic efficiency, however for a certain geometry the interaction probability is an appropriate measure of the detection efficiency [11].

The detector requires cooling but only down to about -30°C and that is provided by a small internal thermoelectric cooling element. The FWHM at 59.5 keV is, according to the manufacturer, 746 eV. The size of the CZT crystal is 3x3x2 mm^3, it is situated behind a beryllium window with a thickness of 250 µm. In the applications employed in this set-up (CT and DPA) narrow X-ray beams only about 3 mm wide are used. Thus the small detector size is ideal for use in this context [12].

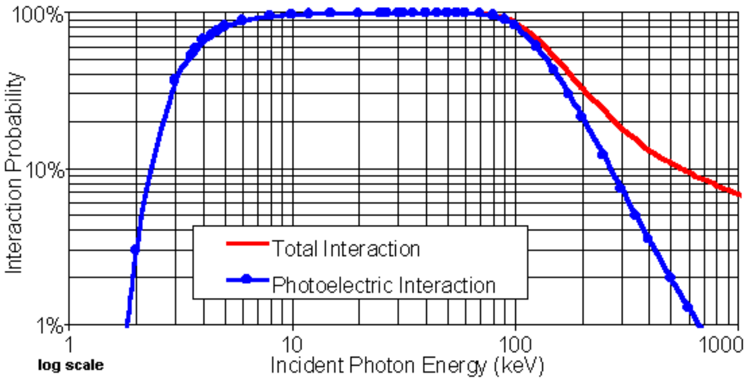

Figure 5.1. Interaction probability as a function of energy for the CZT gamma/X-ray detector used in this demonstrator. Notice the logarithmic scale on both axis.

Since a germanium detector, because of the need of liquid nitrogen cooling, is impossible to use in this application, a comparison between CZT and silicon is interesting. Comparing the photon interaction probabilities of the new CZT with a comparable detector based on the traditional silicon, it is obvious that in the energy range considered (10 – 60 keV) the CZT detector has a significantly higher efficiency, see figure 5.2 [13].

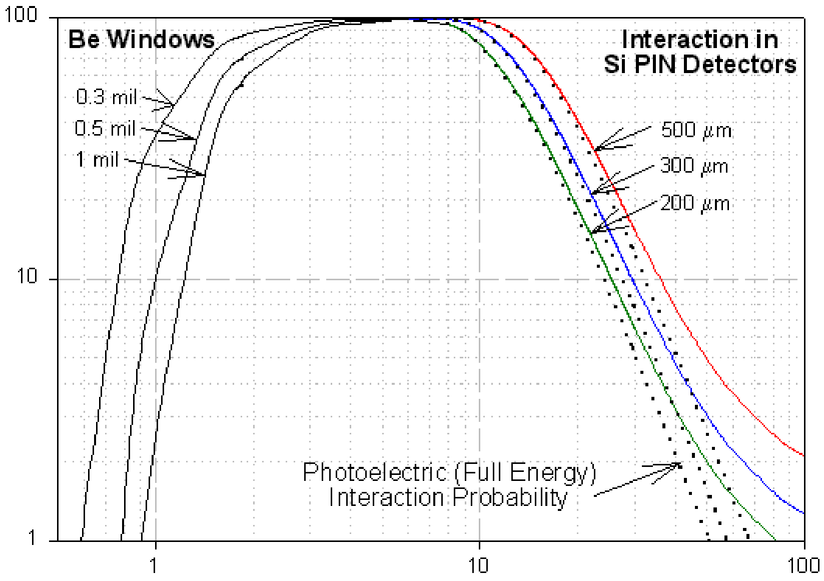

Figure 5.2. Interaction probability in % as a function of energy for a gamma/X-ray detector based on silicon. The different curves represent different thickness of the Be window and the silicon crystal.

The important difference between the figures 5.1 and 5.2 is that in figure 5.2 the interaction probability starts to drop quickly just above 10 keV, while it continues to be close to 100 % all the way up to 90 keV in figure 5.1.

The explanation to this fact lies in the different atomic composition of the two materials. The atomic number of Cd and Te is 48 and 52, respectively, while the atomic number of Si is 14. In the energy range 10-60 keV the photoelectric effect is the dominant mode of interaction and the photoelectric crossection is approximately proportional to Z^5. This is seen in figure 5.3 below, where the linear attenuation coefficient of CZT is compared to that of silicon and germanium.

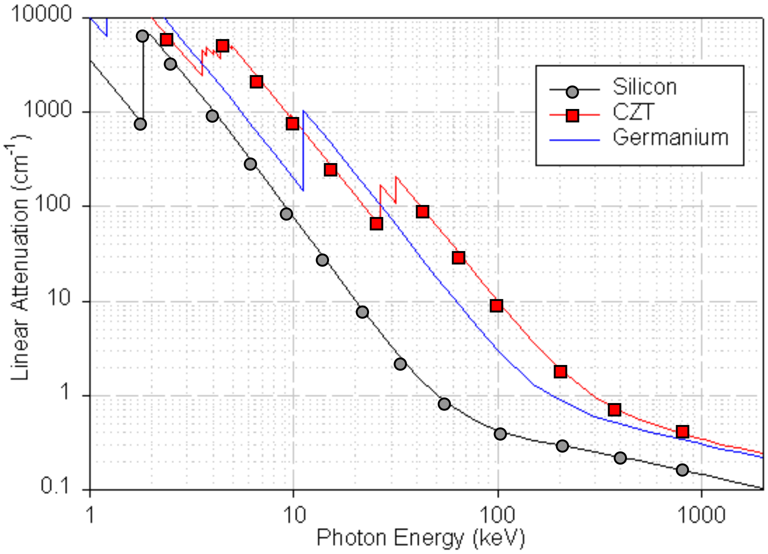

Figure 5.3. Linear attenuation coefficient in cm^{-1} as a function of energy for silicon, CZT and germanium.

The moderate need for cooling of CZT stems from the fact that the band gap of CZT is significantly larger than that of silicon and germanium. That gives a smaller leakage current and hence a better energy resolution for a given temperature [10].

5.4 Defects and trapping

During the process of growing the CZT crystal a number of defects are introduced into the material. When the free charge carriers released in interaction events are transported towards the electrodes these defects act as trapping centres. This means that free charges are captured, trapped, at these sites and recombine with a charge of the opposite sign before they reach the electrode. Due to trapping the number of free charges decays exponentially with time and it is possible to define a certain lifetime for electrons and holes respectively.

For silicon and germanium the density of trapping centres is low and only a negligible fraction of free charges is trapped. CZT on the other hand has a much higher density of trapping centres. Since the mobility of the holes is low, the transit time they need to reach the cathode is much longer than their lifetime and hence the number of free holes is seriously reduced by the presence of trapping centres. Electrons, however, have larger mobility and hence need shorter transit times to reach the anode. The lifetime of free electrons is larger than their transit time and their number is almost unaffected. An interaction taking place near the anode gives a signal that is mainly due to electrons, while an interaction near the cathode gives a signal mainly caused by holes. The effect of trapping is therefor a reduction in the amplitude of the output signal that is strongly dependent on the depth of the interaction site. In the output spectrum this gives rise to a spectral distortion known as ”hole tailing” clearly visible as a tail of events towards lower energies [10].

The detector used in this set-up is, in addition to the standard preamplifier and amplifier, equipped with a device called Rise Time Discriminator (RTD) to reduce these spectral distortions. Since the risetime of the signal is well correlated with the depth of interaction in the detector this device can simply disregard all events occurring below a certain depth by analysing the risetime. In effect the RTD improves spectrum quality at the expense of detection efficiency [10]. At 59.5 keV RTD gives a reduction in detection efficiency of about 20%.

Chapter 6

The ^{241}Am gamma ray source

In this demonstration set-up the X-ray source is not an X-ray tube as in clinical applications used at hospitals but a spontaneously decaying radioactive nuclide producing gamma photons and atomic X-rays in an energy range suitable for medical imaging. There are several reasons for using this source.

- An X-ray tube needs to be operated with some care and it happens now and then that some part breaks down or is worn out, while a radioactive source with suitable half-life needs no maintenance at all.
- A radioactive source is small and light, which is important here since it must be easily moveable in the vertical direction during CT data acquisition.
- The radiation produced by a commercial X-ray tube is of much higher intensity than that emitted by available radioactive sources. In fact the intensity is so high that it would be impossible to register distinct photons in the way that the detector used does.
- The energy spectrum of a radioactive nuclide consists of a number of monoenergetic peaks, while the spectrum from an X-ray tube due to Bremsstrahlung is continuous, covering a wide range of energies. The applications employed in this set-up (CT and DPA) are both performed more easily if the spectrum consists of discrete energy peaks.
- Due to the long acquisition time required for collecting data for a CT image, a photon source of long term stable intensity is required. This requirement is fulfilled by a long-lived radioactive source but perhaps not by a conventional X-ray tube.

6.1 Decay and spectrum

The source is made of the nuclide ^{241}Am (americium), which spontaneously decays to ^{237}Np (neptunium) by emitting an α particle,

$$^{241}\mathrm{Am} \rightarrow {}^{237}\mathrm{Np} + \alpha + 5.638\ \mathrm{MeV}.$$

The half-life of this decay is 432 years. The major part of the energy released in the decay is carried away by the α particle and the rest is used to excite the daughter nucleus (^{237}Np). The excited states of the daughter nucleus in turn deexcite by emitting one or more gamma photons. The states of the ^{237}Np-nucleus are produced and deexcited with different probabilities, resulting in peaks in the gamma spectrum with different intensities. The emitted α particles are stopped in the housing of the americium source so only the gamma photons are detectable. The gamma spectrum of the ^{241}Am source is shown in figure 6.1 below.

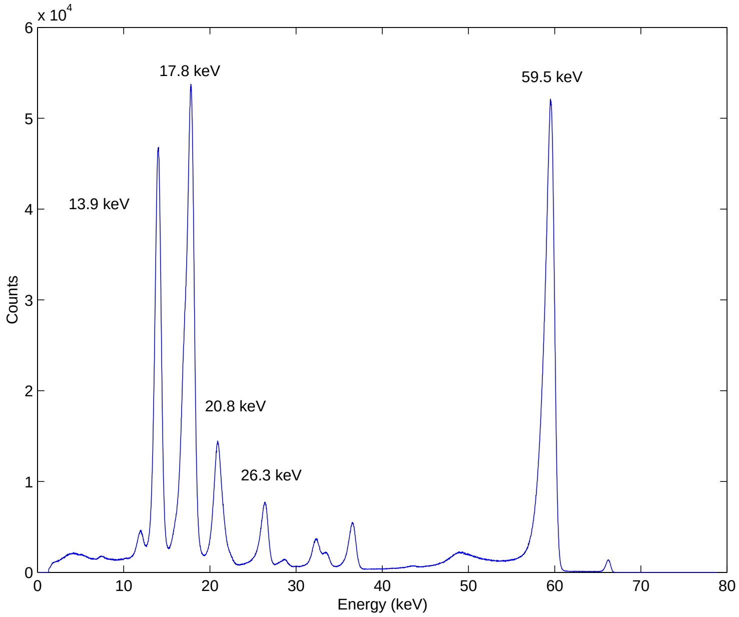

Figure 6.1. Gamma spectrum of the ^{241}Am photon source measured with the CZT detector.

The excited neptunium nucleus can also decay by another process, internal conversion, that competes with gamma emission. In internal conversion the excess energy of the nucleus is transferred directly to an atomic electron. The electron is emitted and leaves a vacancy in one of the atomic shells. This vacancy is soon filled by an electron from one of the outer shells and the difference in binding energy between the two shells is emitted as a photon with an energy in the X-ray range. The radiation produced in this way is the characteristic X-ray spectrum of neptunium. Table 6.1 below shows the energies of the ^{241}Am source and their absolute intensities [3].

Energy (keV)	Intensity (%)
CharacteristicX-rays	
11.9	0.85
13.9	13.3
17.8	19.3
20.8	4.93
Gamma decay	
26.3	2.4
59.5	35.7

Table 6.1. Gamma and X-ray energies emitted from the ^{241}Am source with their respective intensities.

6.2 Activity and shielding

The SI unit for activity is 1 Bequerel (Bq) = 1 decay / second. An older but still commonly used unit is 1 Curie (Ci) = $3.7*10^{10}$ Bq. Radioactive sources commonly used for calibration purposes and in smoke detectors have activities of the order of some µCi and do not require much of radiation protection if handled with care. The activity of this source on the other hand is 10 mCi, that is at least 1000 times stronger and therefor there is definately a need for careful radiation protection. For this purpose the source is mounted inside a tube of solid stainless steel with a thickness of at least one cm in all directions. Due to its density and atomic number (Z = 26) steel is a good absorber of gamma radiation in the energy range 10-60 keV; one cm of steel brings down the intensity of 60 keV photons by a factor of 10^5. No activity originating from the source whatsoever is detectable outside the steel tube. When not in use the opening of the tube in the forward direction, which is a circular hole of 3 mm diameter, is covered by a lid also made of one cm solid steel.

Chapter 7

Description of the set-up

The demonstrator employs two different clinically applied techniques of medical imaging, Computed Tomography and bone mineral density measurement using Dual Photon Absorptiometry. For both techniques some common parts are needed. In addition to the low energy photon source and the detector described in previous chapters, these parts are required: mechanics to be able to scan the beam over the examined object, standard nuclear electronics modules to perform the measurements, a computer to control movements and data acquisition, and finally software to analyse the acquired data set.

7.1 Moving parts

The set-up is designed for examination of objects with a maximum diameter of 9 cm and a maximum length of 20 cm. The detector and the source are mounted co-linearly on a common arm and thus they are always fix in relation to each other. The distance between source and detector is 11 cm. To simplify the mechanics it is not the source-detector-arm that rotates around the object, instead the object is rotated about its centre axis.

The source-detector-arm is perpendicular to the rotation axis of the object and moveable in the vertical direction. It is possible to translate the object in the horizontal direction, along its axis of rotation, to image different crossections. All three movements (rotation as well as translation in the vertical and horizontal directions) are performed by programmable electrical stepper motors, one for each movement. The geometry of the demonstrator is described in figure 7.1 below.

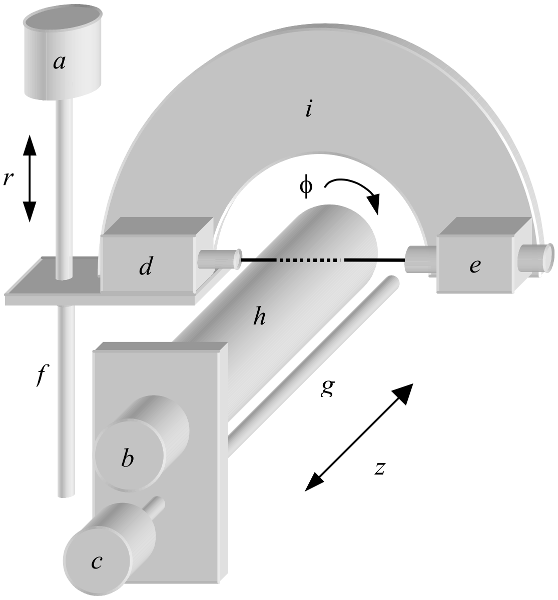

Figure 7.1. Geometry of the source-detector configuration and the moving parts.

In figure 7.1, *a*, *b*, and *c* are the three different stepper motors. When motor *a* is running, the screw *f* rotates and the source-detector arm *i* moves in the vertical direction. When motor *b* is running, the examined object *h* rotates about its centre axis. When motor *c* is running, the screw *g* rotates and the object holder is translated in the horizontal direction. *d* is the CZT detector and *e* is a holder for the cylindrical steel tube that contains the ^{241}Am source. The vertical coordinate is denoted *r*, the horizontal coordinate *z* and the angle of the object is ϕ. A photo of the complete set-up is shown in figure 7.2 below.

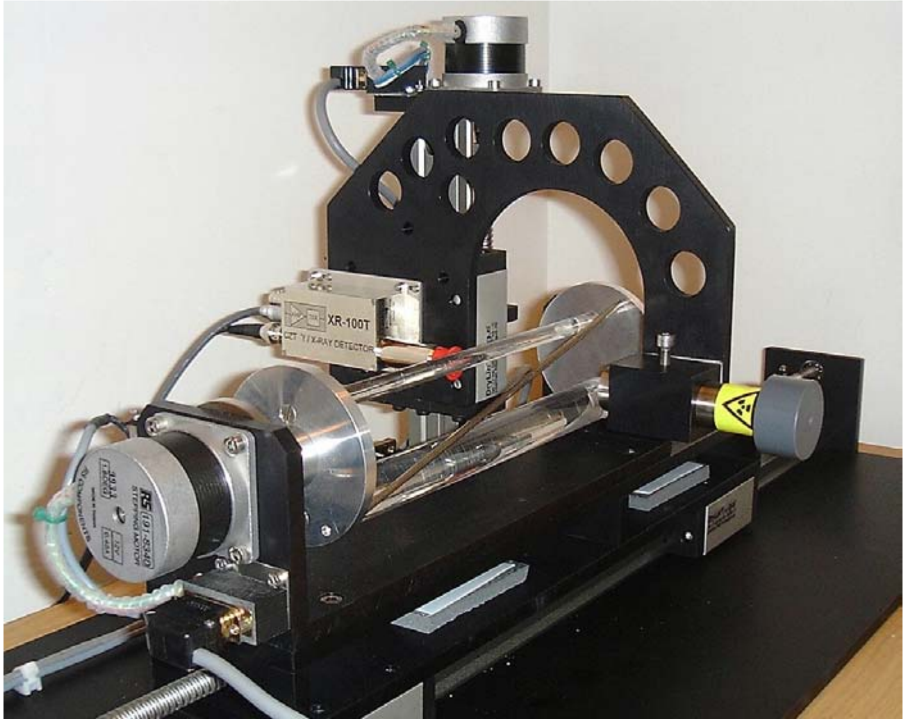

Figure 7.2. Photograph of the demonstrator. Notice the phantom consisting of three different rods as described in section 3.4.

7.2 Electrical stepper motors

The three electrical stepper motors of this set-up can be run in two different ways, either manually or using a computer. These two modes of operation require two different devices, namely a drive board and a control board for each motor. Boards and motors are wired together in a common control unit. Running a motor manually means pressing a switch on the front panel of the control unit, while running it from a computer means connecting it to a control board that, via an RS232 serial port interface, receives instructions from a computer. As opposed to an ordinary electrical motor that is driven by a continuous ac or dc current, these stepper motors are driven by discrete pulses. Feeding the stepper motor each pulse means advancing the rotating axis one discrete step, which in this case is 1.8°, in a certain sense (clockwise or anti-clockwise).

Each stepper motor is connected to a drive board that produces the pulses that drives the motor. When the switch for manually advancing the motor is pressed, pulses are generated at a frequency determined by an oscillator chip mounted on the drive board. The frequency of this oscillator is fairly high so the movement seems continuous. When the motor is controlled by the computer, the internal oscillator chip is replaced by a pulse sequence that the control board, based on the instructions received via its serial port interface, has generated.

7.3 Stepper motor control boards

The computer in this set-up is an ordinary standard PC. The communication between the PC and the two control boards involves sending and receiving text strings via the serial port. The control board is programmable and has a 17 kbyte RAM memory buffer. The basic instructions of the control board are to:

- move a motor to a specified position with a certain velocity
- read out the current position of a motor
- get information about whether a motor is currently moving or not

These instructions are performed by a set of simple commands, which are part of a simplified programming language called RSL. RSL allows the user to write procedure and function definitions that can be downloaded into the memory buffer of the control board. From the computer the user can either call one of the basic built in instructions directly or make a call to a downloaded function or procedure. In this set-up both types of calls are used.

7.4 Nuclear electronics modules

Both measurements performed in this set-up (CT and DPA) make use of discrete photon energies. These energies are selected prior to the measurement with the help of some standard nuclear electronics modules and a PC with a Multi Channel Analyser (MCA) card. The blockdiagram in figure 7.3 below shows the modules used and how they are connected when a narrow energy region, corresponding to a discrete photon energy, is selected. The analogue detector signal is split in two parts. The first part, after passing through an analogue delay unit, goes to the ADC (Analogue to Digital Converter) input of the MCA card. The second part, after processing in an Single Channel Analyser (SCA) and a Gate and Delay Generator (GDG), is fed into the Gate connector of the MCA card.

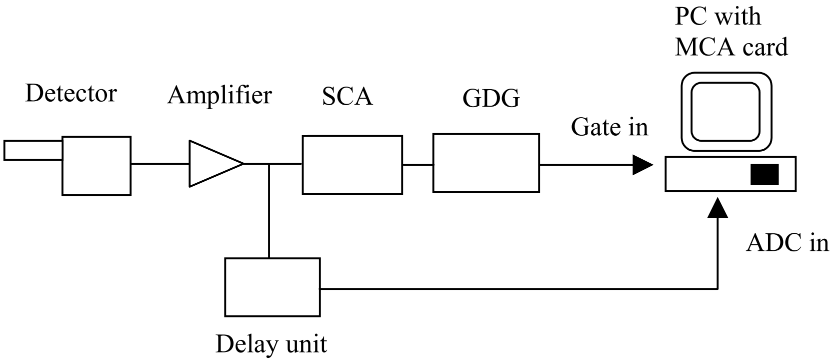

Figure 7.3. Blockdiagram showing the electronics modules used and how they are connected when a discrete photon energy is selected.

The SCA has two independent discriminator levels, a lower level and an upper level. The SCA unit provides a digital signal on its output only if the amplitude of the input signal falls within the window defined by its two discriminator levels. Since the amplitude of the detector signal is proportional to the energy deposited in the detector by the photon, the SCA has the effect of picking out photons of energies only within a certain range. When the MCA card is gated with the digital SCA, only those analogue detector signals that are in coincidence with the SCA signal give a contribution to the output spectrum. By monitoring the output spectrum on the computer screen when adjusting the discriminator levels of the SCA, a certain discrete photon energy is selected for use in CT or DPA data acquisition [4].

The width of the digital pulse on the Gate input of the MCA card must be roughly equal to width of the analogue detector pulse. However in most cases this is not accomplished using the pure output signal of the SCA. A GDG unit is needed to stretch the width of the digital pulse to a desired value.

Since the processing of the signals in the SCA takes some micro seconds, the digital signal is delayed in relation to the analogue signal at the inputs of the MCA card. To compensate for this delay the analogue signal is delayed too. This is performed by an analogue delay unit [4].

During data acquisition the transmitted photon intensity is measured by counting the detected number of photons of a certain energy in a certain time interval. Each detected photon of the desired energy results in a digital pulse from the SCA and these pulses are counted using a scaler. The scaler used is especially designed for this set-up. It has nine different input channels and is controlled and read out using a computer via an RS232 serial port interface. The blockdiagram for counting pulses in discrete energy peaks during data acquisition is shown in figure 7.4 below.

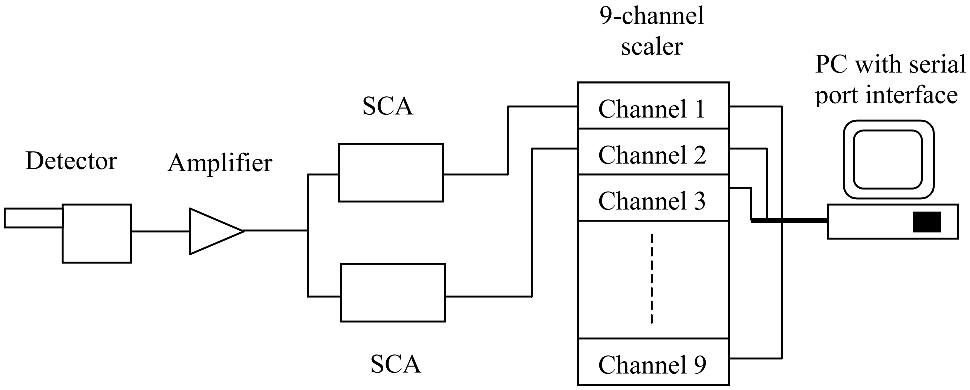

Figure 7.4. Blockdiagram showing electronics modules and connections used when photons of discrete energies are counted during data acquisition.

7.5 Data acquisition procedure

Both the CT and DPA methods involve scanning a narrow photon beam over an area. The intensity of transmitted photons of a certain energy is measured for a number of different positions. As described above the movements of the source-detector arm and the object as well as the reading out of data from the scaler are automated and controlled by a PC, which is the heart of the data acquisition procedure. Since both methods (CT and DPA) require that the position is known with good accuracy, it is important that there is a known correspondence between the intensity and the position values for each single data recorded. In other words the movements of the motors must be closely coordinated with the intensity measurement, which is the main task of the PC. The data acquisition procedure is completely automated by a set of programs written in the LabVIEW programming language. The main outline of the procedure can be summarised in a few steps that are repeated over and over again in a loop over all the measurement positions:

1. The data acquisition program sends a call to the control board to move the stepper motor to a desired measurement position.
2. The program waits while the motor moves to its desired position.
3. When the motor reaches the position the control board sends a verification back to the PC.
4. The data acquisition program tells the scaler to start counting events.
5. The program waits while the scaler is counting.
6. When a specified time has elapsed the data acquisition program orders the scaler to stop counting.
7. The data acquisition program instructs the scaler to read out the contents of the all the scaler channels and send it back to the PC.
8. Acquired data, i.e. the positions of the motors and the contents of the scaler channels, are stored in the primary memory of the PC.
9. Start over from step 1 again.

7.6 PC software

As mentioned above the software needed for data acquisition is written using the LabVIEW programming language. Since the purpose of this set-up is that it shall be used as an educational tool, the programs must have graphical user interfaces that in real time present the data being acquired, that are informative, instructive and easy to understand. Another important thing is flexibility concerning the parameters for data acquisition, like the number of data points and size and position of the object. These things are relatively easy to accomplish using the capabilities of LabVIEW. Besides programs for CT and DPA data acquisition, some other programs for testing the scaler and the stepper motors in a more flexible way have also been written.

For a DPA scan the user simply enters the start and end positions of the region to scan, the distance between consecutive positions and the data acquisition time in each position. Then the data acquisition procedure starts by the click of a button. As more and more data is acquired it is presented in graphical form in real time on the computer screen. For CT data acquisition the operations are similar, though the parameters describing the region to be scanned of course are different.

To make CT imaging more interesting to the student a Barbie doll is examined. Somewhere inside the clothing of the doll is a small steel absorber hidden, a three mm diameter solid steel sphere. The student's task is to find the crossection where the absorber is hidden and make a CT image of that crossection. A LabVIEW program has been written that performs an automated scanning procedure over several different crossections, producing a data set which makes it easy to find a specific crossection containing a strong absorber. During this scanning procedure the source-detector arm is always at the same height as the axis of rotation of the object. For each crossectional plane the object is rotated through half a revolution (180°) and the transmitted intensity is measured for each angle. In that way all points in the crossection are covered by the beam once, provided that the number of angles per 180° is large enough.

When a complete data set for CT or DPA is acquired, another program is needed to perform calculations and analysis of the data. In the case of DPA this involves only simple mathematics, and a program for calculations and analysis could easily be written in LabVIEW. However, for CT the calculations and algorithms needed for image reconstruction are exceedingly more complex. Writing efficient and flexible software for this purpose would definitely be beyond the scope of this diploma work, instead a commercially available product is used. This function is found in the Image Processing Toolbox ver. 2.2.2 of MATLAB ver. 6 and it employs image reconstruction using the Filtered Backprojection algorithm.

Chapter 8

Results

8.1 Counting statistics

As previously described, the photon source of this set-up is not an X-ray tube but a spontaneously decaying radioactive nuclide. Radioactive decay is a statistical process. It is impossible to know when a specific nucleus will decay, all you can say is that it has some probability of decaying per unit time. For all the naturally occurring radioactive nuclides and many of those produced by man this probability per second is a very small number. However even a fraction of a gram of some radioactive material contains at least 10^{15} nuclei. A statistical process like this one where the probability of a single trial is a small number but the number of trials is large is described by the Poisson probability distribution. The number of disintegrations, n, in a given period of time, t , is thus a random variable with a probability distribution

$$P(n) = \frac{(\lambda t)^n e^{-\lambda t}}{n!} \tag{8.1}$$

, where λ is the decay constant - the probability of disintegration per unit time for a single nucleus. It is possible to show that the expectation value of the distribution is [4]

$$\mu = \lambda t \tag{8.2}$$

and that the standard deviation is

$$\sigma = \sqrt{\mu} = \sqrt{\lambda t} \tag{8.3}$$

This means that every time n is measured there is a statistical uncertainty in the value registered and the measure of this uncertainty is the standard deviation. Since the number of registered events, according to equation (8.2), grows linearly with time, while the uncertainty, according to equation (8.3), only grows as the square root of time, long acquisition times are needed to minimise the statistical uncertainty.

As an illustration to the Poisson distribution applied to radioactive decay, consider the number of events needed to achieve a relative statistical error less than 1 %. Let the number of events registered in a certain period of time be N. The relative statistical error s is then

$$s = \frac{\sqrt{N}}{N} = \frac{1}{\sqrt{N}} . \qquad (8.4)$$

The requirement $s \leq 10^{-2}$ hence gives that $N \geq 10^4$[4].

8.2 CT images

8.2.1 Spatial resolution

The spatial resolution of the CT image is dependent on the number of parallel beam projections and the number of data points in each projection. A larger data set means a more detailed description of the depicted object and hence more and smaller pixels, i.e. better spatial resolution. However, by decreasing the distance between consecutive data points, Δr, it is not possible to increase the spatial resolution beyond the width of the beam. Measuring the transmitted intensities at distances closer than the beam width gives no new information. A larger data set of course means longer times needed for data acquisition and image reconstruction.

As mentioned in section 5.3, the front face size of the detector is 3x3 mm^2. The photon beam emerges from a circular hole of 3 mm diameter. The first CT images were acquired using no extra collimation of the beam. The distance between consecutive data points, Δr, was 3 mm while the spacing between different projection angles, $\Delta\phi$, was 3.6°. In an attempt to improve the spatial resolution a steel collimator has been mounted in front of the detector window. The collimator has a circular opening of 1 mm diameter, so the effect is that the beam width is decreased to 1 mm. With this collimator on, CT data sets have been acquired with a distance between consecutive data points of 1 mm and a spacing between different projection angles of 1.8°. Improving the spatial resolution even more would require a smaller collimator and smaller angle steps than 1.8°. The former requirement is in principle possible, although it would require long acquisition times since only a very small part of the available intensity is used. The latter requirement is actually not possible to fulfil with this set-up since the stepper motors cannot move in steps smaller than 1.8°.

As described in section 7.1, a CT image object must fulfil some requirements regarding size to be able to use it in this set-up. Besides, it cannot be too heavy since the stepper motors must be able to rotate it. Only three different objects have been depicted so far. One of them is, as explained in section 3.4, a phantom consisting of three different solid rods. With this object one already knows from the beginning what the crossection should look like, so it is not very exciting for the student to use in the lab exercise. However both the sinogram and the reconstructed image of the phantom are very simple and imaging a known object gives information on how the imaging set-up works. This phantom is hence used as a reference object to verify that the set-up works properly. In figure 8.1 below, a CT image of a crossection of this phantom is shown for two different choices of spatial resolution. One of the corresponding sinograms is shown in figure 8.2.

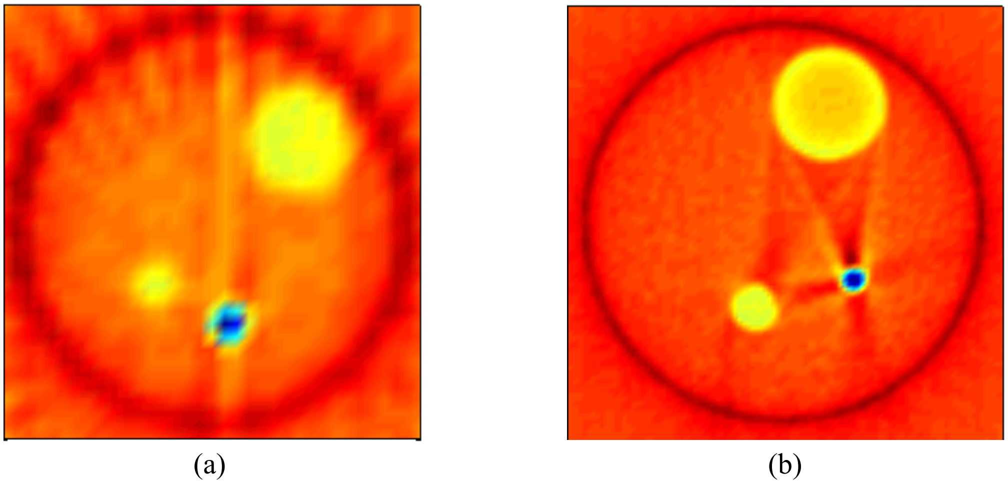

(a) (b)

Figure 8.1a & b. CT images of the three rod phantom at 59.5 keV for two different choices of spatial resolution. In figure (a) Δr = 3 mm and Δϕ = 9°, while in figure (b) Δr = 1 mm and Δϕ = 1.8°.

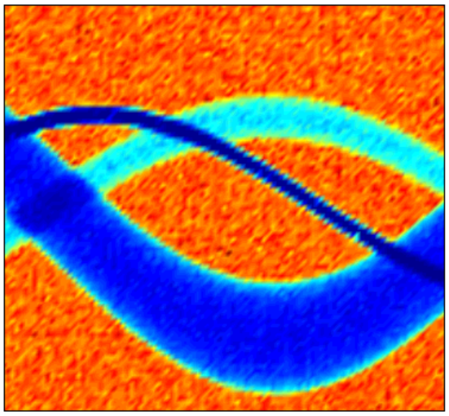

Figure 8.2. Sinogram corresponding to the image reconstruction of figure 8.1b.

In the images above it is obvious that the two thickest rods are made of the same material (plastic), while the thinnest rod is made of a material that absorbs much more (steel). The dark ring surrounding the three rods is not a real object, it just indicates the boundary limit of the data set.

In the sinogram the three different rods are easily distinguishable. The steel rod absorbs more than both the plastic rods despite the fact that it is the thinnest one of them of all. The absorption in the thick plastic rod is greater than in the thin one despite that they are of the same material. All three rods make perfect sine waves over 180°.

8.2.2 Energy selection and contrast level

To make CT imaging more interesting to the students in the lab exercise situation, two other objects can be imaged as well, namely two Barbie dolls. They have the right size, are made of a plastic material that has suitable absorption in the considered energy range, are light and rigid enough to be mounted in the CT set-up. Before any CT images had been acquired the hope was to be able to see the contour of the body and the arms separated from the body.

As mentioned previously (see section 7.4) this demonstrator is capable of acquiring absorption data for several different discrete photon energies. This possibility allows the user to select a data set with an optimal energy for the material composition of the object examined. This feature is illustrated in figure 8.3 below, where a CT image of the male Barbie doll is shown for the energies 17.8 and 59.5 keV, respectively. One of the corresponding sinograms is shown in figure 8.4.

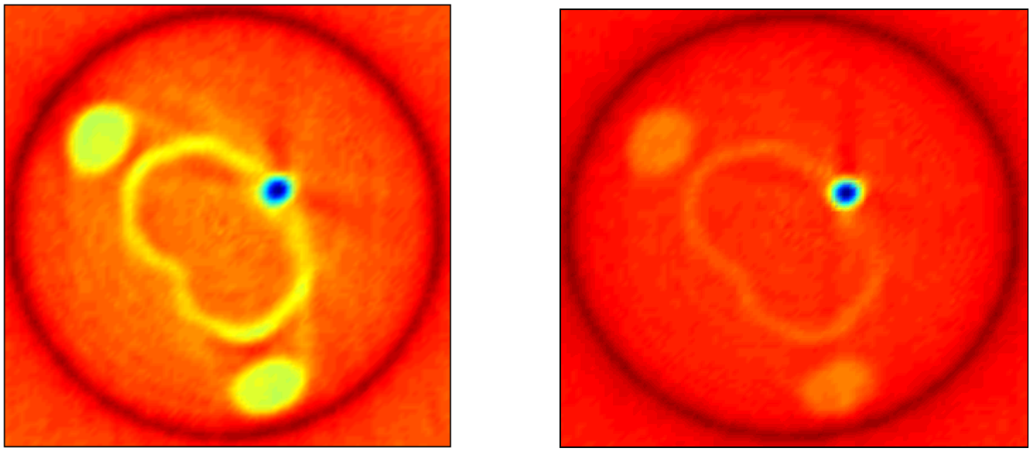

(a) (b)

Figure 8.3a & b. CT images reconstructed from a single data set of two different photon energies, 17.8 keV (a) and 59.5 keV (b). The acquisition time in each data point is two seconds and the spatial resolution is Δr = 1 mm and $\Delta\phi$ = 1.8°.

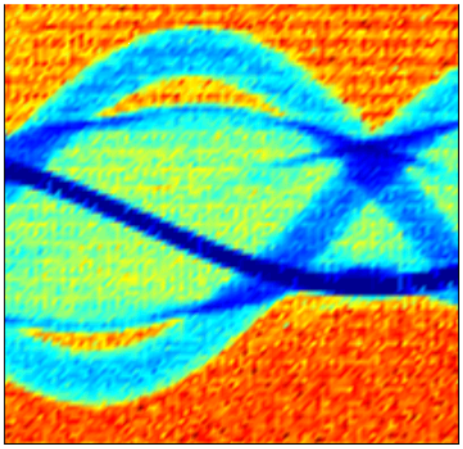

Figure 8.4. Sinogram corresponding to the image reconstruction of figure 8.3a.

To demonstrate the imaging capacity in terms of contrast and spatial resolution, a reference object, a solid steel sphere of 3 mm diameter, has been attached to the front side of the doll. The steel sphere absorbs the low energy gamma radiation almost completely and gives a strong signal clearly visible in both the sinogram and the CT image. It is also seen that the body of the doll is not solid as one perhaps could think, it is just a few mm thick plastic shell and inside is just air. However the arms are made of solid plastic.

The only difference between figures 8.3a and b is the contrast level of the plastic doll in relation to the steel sphere. The reason for this difference is the dependence of the linear attenuation coefficient μ on the photon energy. A simplified model of contrast in X-ray imaging gives the following relation for the contrast level

$$C \propto 1 - exp(-\Delta\mu * x) \qquad (8.5)$$

, where C is the contrast level, x is the thickness of the imaged object and $\Delta\mu$ is the difference in linear attenuation coefficient between the imaged object and the surrounding material. Since the linear attenuation coefficient of a certain material is a function of the photon energy, the contrast level is also varying with energy [5].

Due to higher mass density and higher atomic number, the absorption of X-ray photons is much higher in the steel of the sphere than in the plastic of the doll. At 17.8 keV no detectable radiation whatsoever is transmitted through the steel sphere, while at 59.5 keV a fraction of about 4% of the photon intensity is transmitted. The effect of the strong absorption of the steel is that the number of detected photons when the beam is incident on the steel sphere is zero at both energies. For the plastic of the doll the X-ray absorption is much lower at both energies. This results in a noticeable difference in absorption of X-rays in the plastic doll between the energies of 17.8 and 59.5 keV and this is what gives the difference in contrast between figures 8.3a and b.

8.2.3 Distortions of the reconstructed image

Looking in detail at figure 8.1b, in the background of the image there is a vague pattern of rings centred about the centre of the image. These are artefacts introduced by the image reconstruction algorithm. As mentioned in section 3.3.2 different filter functions are applied to reduce artefacts due to influence of statistical fluctuations. By varying a parameter of a certain filter function the image quality can be improved even further. The filtered backprojection algorithm implemented in MATLAB and used here offers such capabilities of varying the filtering operation. The user can choose between three different types of interpolation (nearest neighbour, linear and spline) and five different filtering functions (Ram-Lak, Shepp-Logan, cosine, Hamming and Hann). There is also a possibility to disregard all spatial frequencies above a certain threshold set by the user.

It turns out that with a suitable choice of filtering options it is possible to achieve noticeable improvements in image quality, both for data sets acquired with high and low spatial resolution. The circular artefacts mentioned above can be greatly reduced by using one of the more advanced filtering functions and by disregarding some of the highest spatial frequencies. Noise in the reconstructed image caused by statistical fluctuations present in the data set can also be reduced by choosing an appropriate filtering function.

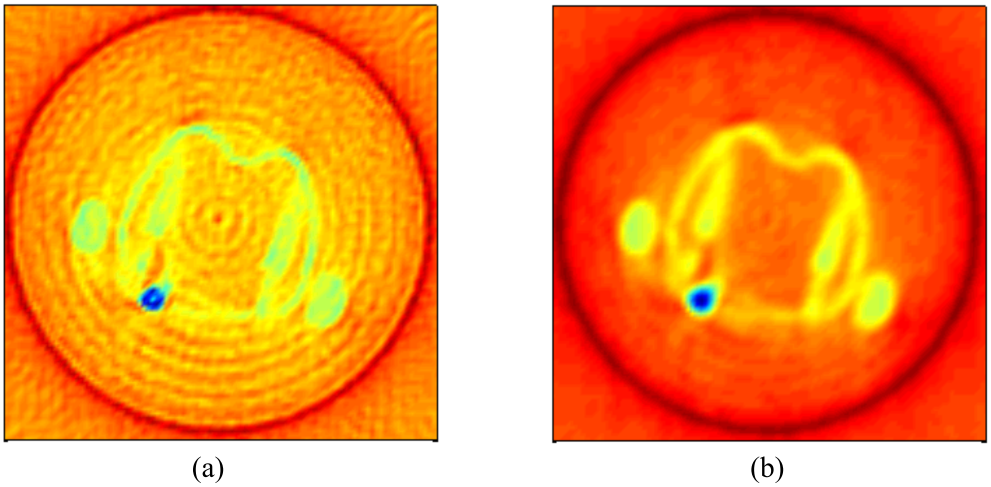
(a)

(b)

Figure 8.5a & b. Two different image reconstructions based on the same data set showing a cross section of the female Barbie doll. In figure (a) a poor choice of filtering options has been used, while in figure (b) the filtering parameters have been optimised. The acquisition time in each data point is two seconds and the spatial resolution is $\Delta r = 1$ mm and $\Delta\phi = 1.8°$.

The image to the left (8.5a) is reconstructed using the simplest filtering function available, the Ram-Lak filter, and all spatial frequencies are included in the calculation. The image to the right (8.5b) is reconstructed with one of the more advanced filtering functions, the Hamming filter, and the highest 40% of the spatial frequencies are excluded from the calculation. In figure 8.5a two different distortions are visible, a pattern of concentric circles as well as noise resulting from statistical fluctuations. The filtering operation applied when calculating figure 8.5b has greatly reduced these two distortions at the expense of blurring the image [5].

8.2.4 Acquisition time

The software performing the automated data acquisition procedure allows the user to make a large number of combinations of data acquisition parameters. The angle between consecutive projections ($\Delta\phi$), the distance between data points (Δr) and the acquisition time in each position can all be varied independently. For a certain examined object, the choice of these parameters affects the total acquisition time. If the object is massive and made of a material that has high absorption or if the collimator is used, then a longer acquisition time in each position is needed to achieve a reasonably low statistical error. Table 8.1 below shows the total acquisition times for two different choices of acquisition parameters when the diameter of the field of view is 96 mm. The number of detected photons in each data point, and hence the statistical uncertainty, is roughly the same for both these cases.

Δr (mm)	$\Delta\phi$	Collimation	Acquisition time in each position (s)	Total number of data points	Total acquisition time
3	3.6°	no	0,5	1600	1 h 10 min
1	1.8°	yes	2,0	10^4	8 h

Table 8.1. Two different choices of acquisition parameters and the resulting total acquisition time for a field of view diameter of 96 mm. Δr is the distance between consecutive measurement positions in the vertical direction, $\Delta\phi$ is the angle between consecutive projections, collimation refers to whether to the steel collimator is mounted in front of the detector window or not.

The total acquisition time for a CT slice depends on the number of measuring positions, the acquisition time in each position and the transport time of the source-detector arm.

8.3 Bone Mineral Density profiles

For measurement of Bone Mineral Density profiles two different blocks of solid material and rectangular shape have been used. One of the blocks is a piece of a skeletal bone from a cow and the other is a piece of a paraffin. The block of bone has a thickness of 4.3 mm while the paraffin block is 35 mm thick. When data for bone mineral density measurement with the Dual Photon Absorptiometry method is acquired, the paraffin block is used to simulate the soft body tissue surrounding the bone in some part of the body. The two blocks are placed in front of each other according to figure 8.6 below.

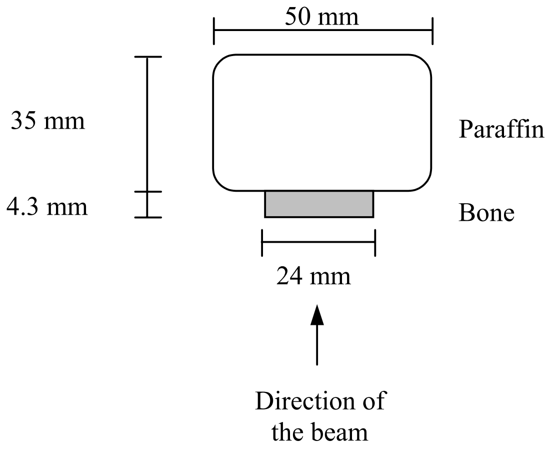

Figure 8.6. The two blocks of bone and bone and paraffin as seen from above.

The raw data acquired from a DPA scan is two X-ray intensity profiles, an example is given in figure 8.7 below.

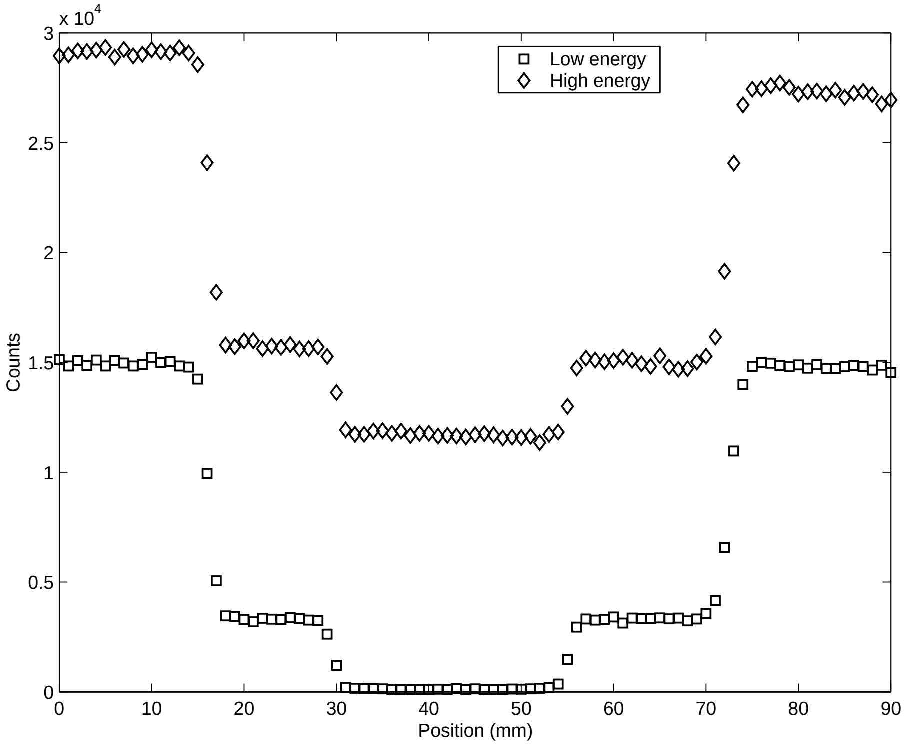

Figure 8.7. The two X-ray intensity profiles acquired from a DPA scan across the two blocks shown in figure 8.6.

The two profiles show the transmitted intensities of two different discrete photon energies emitted by the ^{241}Am source, namely 17.8 and 59.5 keV. In figure 8.7 both profiles can be divided into five different regions where the inten§sity is constant. In each of these regions the beam is attenuated by a constant thickness of some combination of air, paraffin and bone, see table 8.2 below.

Region (mm)	Material
0-15	Air
16-30	35 mm of paraffin
31-55	35 mm of paraffin and 4.3 mm of bone
55-72	35 mm of paraffin
73-90	Air

Table 8.2. The materials in the different regions of the profiles presented in figure 8.7.

Referring to figure 8.7 it is obvious that in the air region, the intensity of the 59.5 keV photons is higher than that of the 17.8 keV photons. This is a consequence of the features of the gammaspectrum of the ^{241}Am photon source. More photons are simply emitted per unit time at 59.5 keV than at 17.8 keV, see the spectrum of figure 6.1.

To be able to calculate the areal densities of bone and soft tissue (here simulated by paraffin) from equations (4.6a) and (4.6b), the four mass attenuation coefficients μ_s', μ_b', μ_s and μ_b must be known. These quantities are easily determined by measuring the absorption of photons of two discrete energies in the blocks of bone and paraffin respectively. Since the thickness and mass density of both samples is known, the mass attenuation coefficient is obtained by inverting equation (2.5) and normalising with the density, which gives

$$\mu = -1/(\rho x)*ln(I(x)I(0)). \qquad (8.6)$$

Using equation (8.6) these values of the four mass attenuation coefficients have been calculated: $\mu_s' = 0.483$ cm^2/g, $\mu_b' = 5.22$ cm^2/g, $\mu_s = 0.197$ cm^2/g, and $\mu_b = 0.395$ cm^2/g,. Here, as in equations (4.6a) and (4.6b), primed primed variables denote the low energy, unprimed denote high energy and indices *s* and *b* refer to soft tissue and bone respectively.

Applying equations (4.6a) and (4.6b) to the absorption profiles measured at 17.8 and 59.5 keV respectively yields the two areal density profiles shown in figure 8.8 below.

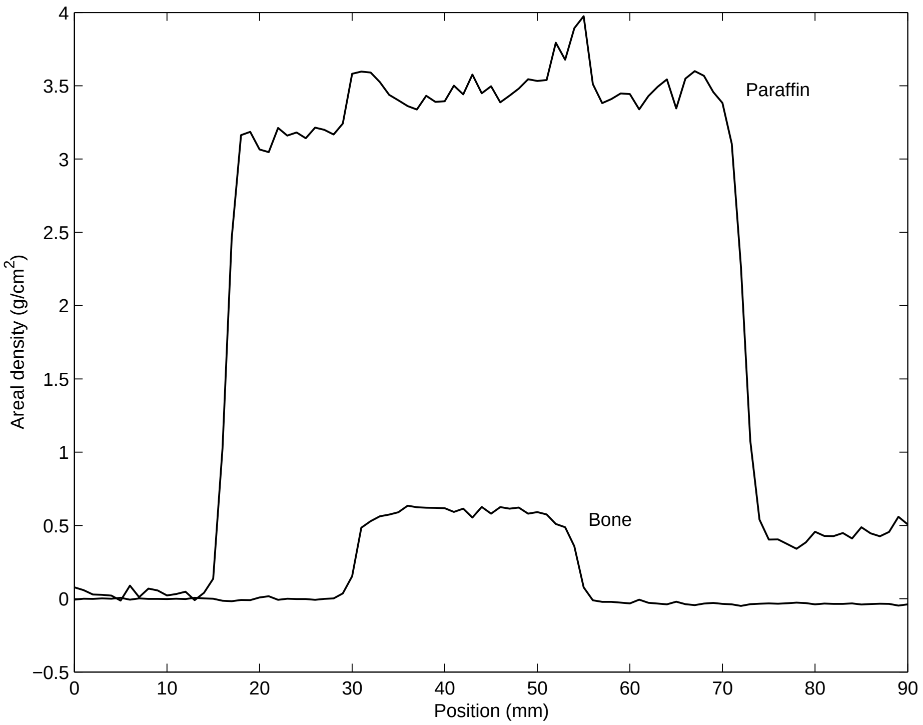

Figure 8.8. Areal densities in g/cm^2 of bone and paraffin calculated from the profiles presented in figure 8.7.

Comparing the calculated areal densities of bone and paraffin shown in figure 8.8 with the actual distribution of materials according to table 8.2, the result is as expected. In the region 31-55 mm the areal density of bone is constant at a level of 0.6 g/cm^2, everywhere else it is zero. Since the thickness of the bone sample is 0.43 cm and the mass density of it is 1.8 g/cm^3, this is a value roughly in agreement with the expected. The areal density of paraffin is constant at a level of 3.1 g/cm^2 in the region 16-72 mm and zero everywhere else. With a thickness of the paraffin sample of 3.5 cm and a mass density of 0.89 g/cm^3, this is in good agreement with what is expected.

References

1. Blake, G.M., Wahner, H.W., Fogelman, I. The evalution of Osteoporosis second edition (1999): Martin Dunitz.
2. http://www.nobel.se/medicine/laureates/1979/press.html, 2001. Official Web Site of the Nobel Foundation.
3. Krane, Kenneth S. Introductory Nuclear Physics (1988): Wiley.
4. Leo, W.R. Techniques for Nuclear and Particle Physics Experiments 2nd rev. ed (1994): Springer Verlag.
5. Webb, S. The Physics of Medical Imaging (1996): IOP.
6. Farr, R.F., Allisy-Roberts, P.J. Physics for Medical Imaging (1999): Saunders.
7. Bushberg, J.T., Seibert, J. A., Leidholt, E.M. Jr., Boone, J.M. The essential physics of medical imaging (1994): Williams and Wilkins.
8. Jacobson, Bertil. Medicin och teknik (1995): Studentlitteratur.
9. Shung, K.K., Smith M.B., Tsui, B. Principles of medical imaging (1992): Academic press.
10. Redus, Bob. Charge Trapping in XR-100T-CZT Detectors (2000), Amptek application note.
11. Amptek Inc. Efficency of XR-100T-CZT Detectors (2000), Amptek application note.
12. Amptek Inc. Operating Manual XR-100T-CZT X-ray and gamma ray detector system (2000).
13. http://www.amptek.com/, 2001. Amptek Inc.